PROCEEDINGS OF SPIE

Design of the VLTI/Hi-5 light injection system

G. Garreau, A. Bigioli, G. Raskin, J.-P. Berger, C. Dandumont, et al.

SPIE.

Design of the VLTI/Hi-5 light injection system

G. Garreau[a], A. Bigioli[a], G. Raskin[a], J-P. Berger[b], C. Dandumont[c], H-D. Kenchington Goldsmith[d], S. Gross[e], M. Ireland[d], L. Labadie[f], R. Laugier[a], J. Loicq[c,g], S. Madden[d], G. Martin[b], A. Mazzoli[c], J. Morren[a], H. Shao[d], K. Yan[d], and D. Defrère[a]

[a]Institute of Astronomy, KU Leuven, Celestijnenlaan 200D, 3001 Leuven, Belgium
[b]Univ. Grenoble Alpes/CNRS, IPAG, F-38000 Grenoble, France
[c]STAR Institute, University of Liège, 19C allée du Six Août, 4000 Liège, Belgium
[d]Research School of Astronomy & Astrophysics, Australian National University, Canberra, ACT 2611, Australia
[e]MQ Photonics Research Centre, School of Mathematical and Physical Sciences, Macquarie University, NSW, 2109, Australia
[f]I. Physikalisches Institut, Universität zu Köln, Zülpicher Str. 77, 50937 Köln, Germany
[g]Faculty of Aerospace Engineering, Delft University of Technology, Kluyverweg 1, 2629 HS Delft, Netherlands

ABSTRACT

Hi-5 is an ERC-funded project hosted at KU Leuven and a proposed visitor instrument for the VLTI. Its primary goal is to image the snow line region around young planetary systems using nulling interferometry in the L' band, between 3.5 and 4.1 µm, where the contrast between exoplanets and their host stars is very advantageous. The breakthrough is the use of a photonic chip based beam combiner, which only recently allowed the required theoretical raw contrast of 10^{-3} in this spectral range. The VLTI long baseline interferometry enables to reach high angular resolution (4.2 mas at 3.8 µm wavelength with the Auxiliary Telescopes (ATs)), while high contrast detection is achieved using nulling interferometry. This polarisation requires a high degree of optical symmetry between the four pupils of the VLTI, only possible with precise phase, dispersion and intensity control systems. The instrument is currently in its design phase. In this paper, the warm optics design and the injection system up to the photonic chip are presented. The different properties of the design are presented including the optics used, the characteristics of the four beams and the current drawbacks. Particular attention is devoted to the optical alignment and the tolerance analysis in order to estimate the precision required for the alignment procedure and therefore to choose adapted optical mountings.

Keywords: Instrumentation, nulling interferometry, VLTI, Hi-5

1. INTRODUCTION

Imaging planetary systems close to the snow line is an important step in astronomy. This region is known to be statistically rich in exoplanet distribution[1]. Long baseline interferometry already manages to probe exoplanets using high angular resolution (∼50 mas) and high contrast ($\sim 10^{-4}$) with the GRAVITY instrument[2] at the Very Large Telescope Interferometer (VLTI). Another solution to reach high contrast is to use nulling interferometry first presented by Bracewell in 1978[3] and already implemented for example with the Palomar Fiber Nuller (PFN)[4], the Keck Interferometer Nuller[5] or the Nulling and Imaging Camera (NIC)[6] at the Large Binocular Telescope (LBT). Hi-5 is a nulling interferometer[7] proposed for the VLTI as part of the Asgard instrument suite[8] dedicated to high contrast imaging[9]. The instrument would be the first one to implement nulling interferometry at the VLTI, achieving a contrast of 10^{-5} after self-calibration. It will use a photonic chip-based beam combiner already successfully implemented for other interferometric instruments like in VLTI/PIONIER[10] or Subaru/GLINT[11]; it enables a more stable and more compact design as well as an easier alignment procedure than free-space optics. The innovation brought by Hi-5 is the use of such integrated optics in the L' band

---

Further author information: Germain Garreau: E-mail: germain.garreau@kuleuven.be

[3.5-4.1] µm, a spectral region where guided optics is still fledgling[12] . The coupling between free space beams with imperfect wavefronts and guided mode requires a careful engineering for the injection system. On top of this challenge, nulling interferometry is indeed particularly demanding when it comes to the symmetry between the different beams. This work is presenting the current design for the injection system of Hi-5 including the different requirements that need to be fulfilled (Sec. 2), the optical design realized on Zemax (Sec. 3) and finally its corresponding tolerance analysis (Sec. 4).

2. REQUIREMENTS FOR THE INJECTION SYSTEM

In this section, we define the main requirements that need to be considered for the design of the injection system: the intensity, the polarisation and the phase. The studies on the polarisation and the phase will not be further developed in this work as they are still in progress.

2.1 Description of the photonic chip-based beam combiner

The studied photonic chip-based beam combiner (or "chip") is an integrated optic fabricated from a dielectric substrate where an Ultrafast Laser Inscription (ULI) changes the refractive index of the material locally to create optical waveguides[13] . The use of couplers inside the chip enables to generate interferences by evanescent coupling between the different waveguides (see Fig. 1) .
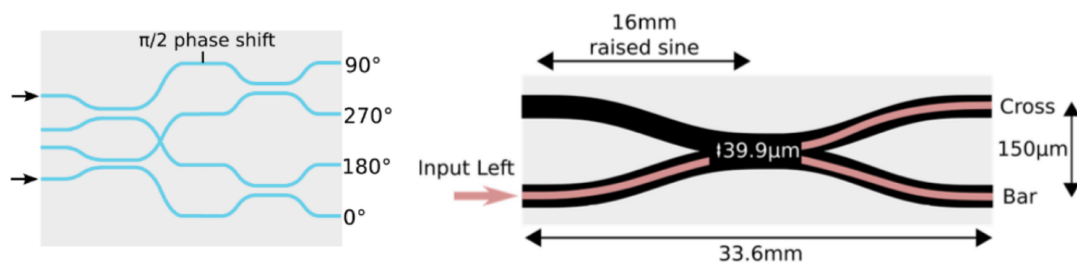

Figure 1. (left) Example of a 4-Telescopes ABCD photonic beam combiner design. (right) Detailed structure of a photonic coupler. Source:[13]

The chip planned to be used in the Hi-5 instrument is made of Gallium Lanthanum Sulfide (GLS) Chalcogenide glass with propagation losses as low as $0.22\,\mathrm{dB/cm}$ at $4\,\mu\mathrm{m}$ wavelength[14] . This chip is realized at Macquarie University and it has four inputs corresponding to the four telescopes of the VLTI with the following optical properties for each input:

$$\begin{cases} \text{Numerical Aperture (NA)} \simeq 0.1 \\ \text{Core diameter} \simeq 20\,\mu\mathrm{m} \\ 1/\mathrm{e}^2 \text{ Mode Field Diameter (MFD)} \simeq 22\,\mu\mathrm{m}\,@\lambda{=}4\,\mu\mathrm{m} \\ \text{Input Separation} \simeq 125\,\mu\mathrm{m} \end{cases} \tag{1}$$

After its manufacturing, the chip is being tested at Universität zu Köln[12] .

2.2 Objective

The VLTI observatory is transmitting the signal as collimated beams with a diameter of 18 mm and a separation of 240 mm from its four Unit Telescopes (UT). These beams are first expected to go through the Asgard/Heimdallr[15] fringe tracker with adapted optics mirrors that will change the beam diameter to 12 mm. The challenge is therefore to inject these 12 mm-diameter beams into the four inputs of the chip combiner with maximum optical throughput and minimum null depth.

2.3 Requirements on the coupling efficiency

2.3.1 Coupling efficiency definition

The coupling efficiency ρ corresponds to the ratio of energy between the incoming beam and the light that actually couples and propagates into the waveguide. Its expression is described in[16]

$$\rho = \frac{|\iint F_r(x,y)W^*(x,y)dxdy|^2}{\iint |F_r(x,y)|^2 dxdy \iint |W(x,y)|^2 dxdy} \quad (2)$$

with F_r and W the complex amplitudes of the receiving input mode(s) and the coupling beam respectively. When simplifying the problem by considering a gaussian approximation for F_r and an Airy pattern from diffraction-limited regime for W, a simpler expression for the coupling efficiency is obtained from[17]

$$\rho = 2 \left[\frac{e^{-\beta^2} - e^{-\beta^2 \alpha^2}}{\beta \sqrt{1-\alpha^2}} \right] \quad (3)$$

$$\text{and:} \quad \beta = \frac{\pi}{2} \frac{\omega_0}{\lambda} f_\# \quad (4)$$

with α the central obstruction, ω_0 the mode diameter of the waveguide, λ the wavelength of the beam and $f_\#$ the f-number of the input. The resolution of this equation with no obstruction ($\alpha = 0$) gives an optimal value of $\rho \simeq 81\%$ for $\beta = 1.1209$, which corresponds to $f_\# \simeq 0.13 @ \lambda = 4\,\mu m$.

2.3.2 Requirement on the coupling efficiency

The objective for each individual input is to maximize the coupling efficiency (see Eq. 2) with a minimum value of 75%. This value is very sensitive to aberrations, alignment and wavefront errors caused by the injection system and a tolerance analysis is performed in Sec. 4 to evaluate it.

2.4 Requirements on the null depth

2.4.1 Null depth definition

The null depth of the instrument corresponds to the ratio between the stellar flux transmitted to the null output (or stellar leakage) and the total stellar flux collected by the telescopes. A lower null depth enables to detect fainter companions around the host star. To achieve its science goals[18], Hi-5 has an objective of a raw null depth $N_{\mathrm{raw}} \leq 10^{-3}$ and a calibrated null accuracy $N_{\mathrm{calibrated}}$ of 10^{-5}. This value is very sensitive to asymmetries between the different beams in terms of intensity, polarisation or phase. To achieve $N_{\mathrm{raw}} \leq 10^{-3}$, these sources of asymmetry should all individually aim for a null depth $\leq 10^{-4}$ as a safe margin.

2.4.2 Impact of the relative intensity error

The relative intensity error between the inputs σ_I is capping the null depth N_I[19]

$$N_I > \sigma_I^2. \quad (5)$$

The aimed relative intensity error is then $\sigma_I \leq 1\%$ for a null depth of $N_I > 10^{-4}$ according to Eq. 5. The tolerance analysis in Sec. 4 also evaluates the impact of the injection system on N_I.

2.4.3 Impact of the polarisation

Relative polarisation asymmetries, both static and dynamic, are hampering the null depth of the instrument. In the injection system, this asymmetry may arise from a differential TE/TM phase delay between the different beams. The relative polarisation rotation angle between the inputs α_{rot} is capping the null depth of the instrument N_P with[19]

$$N_P > \frac{\alpha_{rot}^2}{4}. \quad (6)$$

This angle should be kept at $\alpha_{rot} \leq 0.02$ rad in order to have a null depth $N_P > 10^{-4}$ according to Eq. 6 (see Fig. 2). The injection system has to reduce as much as possible the differential delay between the TE/TM polarisations, for example by reducing the relative angle between the mirrors of the different arms in the instrument. A system of birefringent waveplates also has to be implemented in the future to perform both static and dynamic polarisation control.
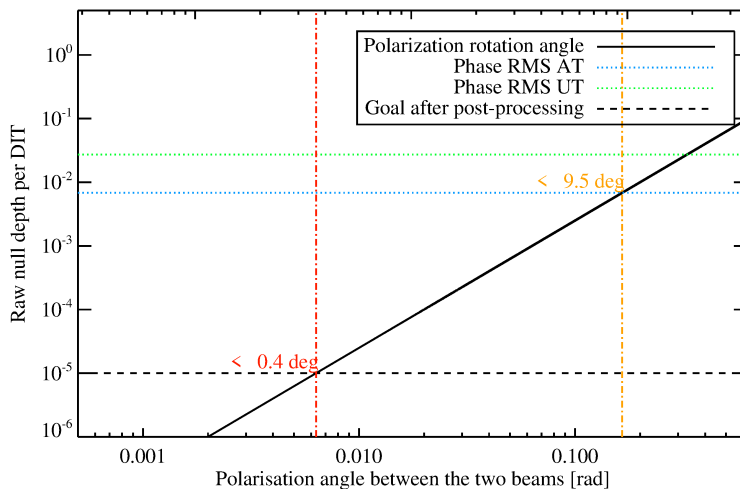

Figure 2. Impact of the polarisation angle error on the raw null depth and comparison with the impact of phase error, assuming 100 nm RMS for the ATs and 200 nm RMS for the UTs[20].

2.4.4 Impact of the phase

The relative phase difference between the four beams may have various sources: mainly the Optical Path Delay (OPD) and the longitudinal dispersion from water vapor[21]. The OPD represents the difference of optical path Δx between two light beams. The associated phase difference $\Delta \phi$ scales with the optical frequency ν as

$$\Delta \phi = 2\pi n \nu \frac{\Delta x}{c} = 2\pi n \frac{\Delta x}{\lambda} \tag{7}$$

with c, the speed of light in vacuum and n, the refractive index of the medium of propagation. After correction of the static phase difference, the total relative phase fluctuation σ_ϕ is capping the null depth N_ϕ[19]:

$$N_\phi > \sigma_\phi^2. \tag{8}$$

Even though Hi-5 is planned to include internal delay lines to correct the static piston effect (from static OPD), this correction can only go up to $\sim$12 mm. The injection system design thus has to implement the four arms of the interferometer with no static OPD to simplify this static correction. The fast variations of OPD are corrected by the Asgard/Heimdallr fringe tracker beforehand.

3. DESIGN OF THE INJECTION SYSTEM

In this section, we provide a description of the injection system optical design and the technical challenges faced for its realization.

Fig. 3 shows a detailed schema of the injection system optical design realized on Zemax. The four beams coming from the VLTI arrive parallel and collimated with a diameter of 12 mm after the Heimdallr fringe tracker and are focused via four identical Off-Axis Parabolas (OAP) onto an Intermediate Image Plane (IIP). The use
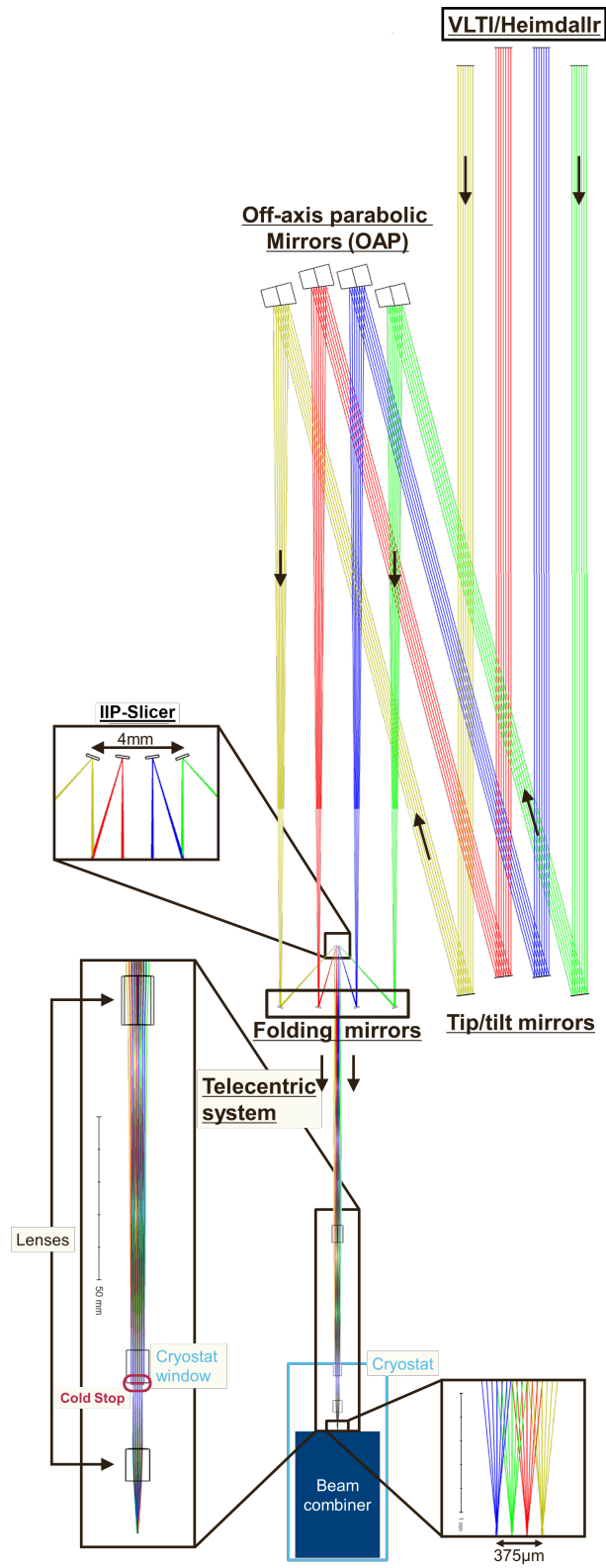
Figure 3. Design of the injection system on Zemax considered in this study.

of four identical OAP is motivated by the need of high symmetry between the arms of the interferometer. The focal length of these OAP can be customized if necessary but in our case the optical design was chosen to match with standard (or commercially available off-the-shelf) OAP parameters.

$$\text{\underline{OAP parameters:}} \left\{ \begin{array}{l} f_{\text{OAP}} = 646\,\text{mm} \\ D_{\text{OAP}} = 25.4\,\text{mm} \\ \text{Angle}_{\text{OAP}} = 15\,\text{deg} \end{array} \right. \tag{9}$$

Since the four OAP share the same angle, folding mirrors are being added to the design in order to direct the beams towards the IIP. Once in the IIP, additional mirrors called "slicer" (as a reference to the slicer used in integral field spectroscopy) are orienting the beams towards the chip combiner. The injection in the chip is performed for a separation of 125 µm between each inputs, as such it is necessary to magnify this separation in the IIP in order to relax the spatial constraints on mirrors and optical mountings. This magnification is performed using a telecentric system with two lenses in Zinc Selenide (ZnSe): a collimation aspherical lens and a telecentric lens (see Fig. 4).

$$\text{\underline{Telecentric lens:}} \left\{ \begin{array}{l} f_{\text{telelens}} = 20\,\text{mm} \\ D_{\text{telelens}} = 7.5\,\text{mm} \\ t_{\text{telelens}} = 10\,\text{mm} \\ \text{Conic}_{\text{telelens}} = -0.4 \end{array} \right. \quad ; \quad \text{\underline{Collimation lens:}} \left\{ \begin{array}{l} f_{\text{collilens}} = 230\,\text{mm} \\ D_{\text{collilens}} = 10\,\text{mm} \\ t_{\text{collilens}} = 15\,\text{mm} \\ \text{Conic}_{\text{collilens}} = 6.8 \end{array} \right. \tag{10}$$

The magnification value corresponds to the ratio of focal lengths $M = \frac{f_{\text{collilens}}}{f_{\text{telelens}}}$ which needs to be maximized in order to have less constraints on the optics located at the IIP. In the current situation, the magnification obtained from Eq. 10 is $M \sim 11$ which gives a beam separation of 1.33 mm in the IIP.
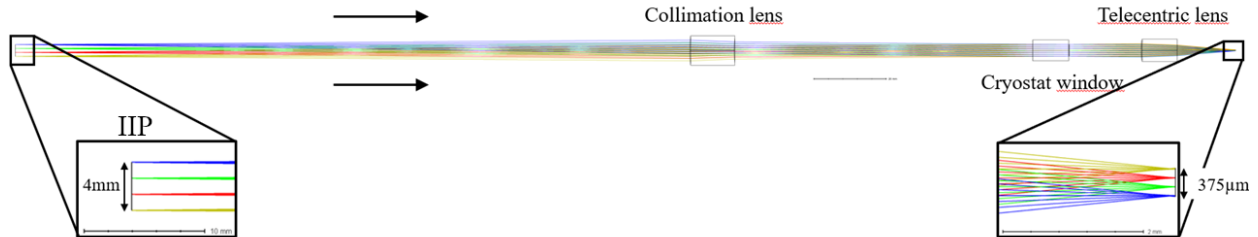

Figure 4. Full telecentric system design on Zemax.

A telecentric system is an optical system which has one of its pupil located at infinity resulting in a low dependency of the image to the angle of incidence of the incoming beams. In our situation, the exit pupil is located at infinity to allow all the light going through the aperture stop to be injected into the chip. To place the exit pupil at infinity, the aperture stop of our system must be located at the focal plane of the telecentric lens like in Fig. 5.
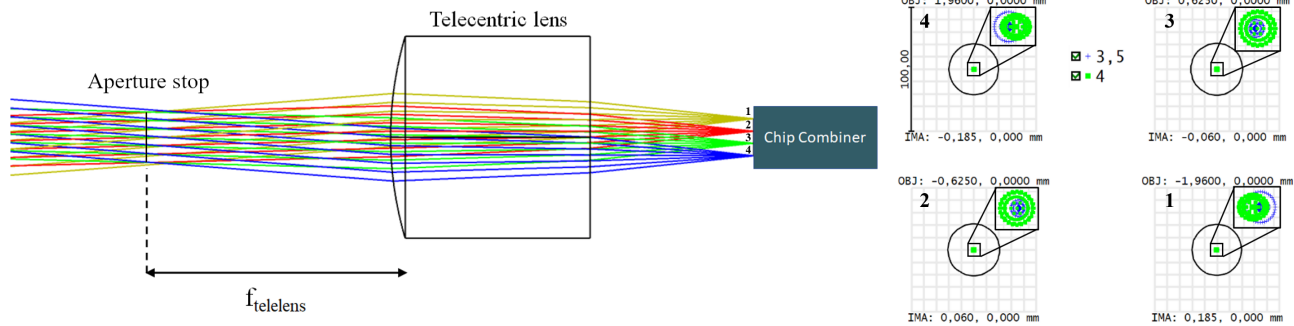
Figure 5. (left) Example of a telecentric lens for a four beam injection in the chip combiner. (right) Results in the image plane with the spot diagram of the four beams, the black circle corresponds to the Airy disk associated with the wavelength and $f_\#$ of the lens.

In the L' band, between 3.5 and 4 µm wavelength, every object at ambient temperature is emitting significant thermal light. It is then necessary to mitigate this background emission from the light that we inject into our photonic component. The usual solution in that case is to place the aperture stop from Fig. 5 at the pupil plane inside a cryostat to block this light from reaching the inputs of the chip. We therefore call it "cold stop". As a safe margin, the cold stop diameter is usually chosen to be slightly smaller than the pupil diameter of the beams thus insuring an optimal reduction of the background flux. A pupil matching also needs to be performed by overlapping the exit pupil from the collimation lens, the entrance pupil of the telecentric lens and the cold stop. This pupil matching is important to make sure that the background is properly filtered from the signal and that no loss from vignetting is reducing the intensity from the telescope.

For the telecentric lens position to the chip, two solutions are possible: the first solution would be to directly glue the lens to the chip. This solution has the benefits of being more robust and would offer an easier alignment for the injection system. The second solution with a detached lens would put less constraints on the size, thickness and focal length of the lens but would also make the alignment with the chip more complex. The key parameter to consider here is the numerical aperture for the four inputs of the chip that is worth NA = 0.1. In the case of a glued lens, the medium of propagation is in ZnSe with a refractive index n $\simeq$ 2.4 in the L' band. Considering that the maximum thickness of a manufactured glued lens is $\simeq$ 1 cm, this induces an cold stop diameter $D_{CS} \simeq 0.834$ mm. Such a diameter for a cold stop makes the alignment difficult and since increasing the thickness of the lens above 1cm would make its manufacturing risky, the option of a detached lens as in Fig. 4 becomes default to respect NA = 0.1. The detached telecentric lens position is chosen to allow a cold stop diameter $D_{CS} = 4$ mm corresponding to the pupil diameter after the collimation lens.

Fiber injection vs direct injection:

For light injection into a photonic chip devoted to astronomical interferometry, two methods are generally used: the first and most common one consists of attaching optical fibers through v-groove fiber arrays to the inputs and injecting the beams through the fibers; this is the case for the instruments PIONIER[10], IOTA[22] or GRAVITY[23] for example. The second one consists of using a direct injection setup with lenses or micro-lens array to focus the light beams on the different inputs as in the GLINT[11] example. The first method with optical fibers has the benefit of being stable and easier to align and inject in the chip. However as Hi-5 is an instrument performing in the mid-infrared (in the L' band specifically), the chip combiner has to be placed inside a cryostat to reduce the background. To this day, standard MIR fibers are not adapted to low temperatures; their attachment to the chip would therefore require a long and expensive development phase. The second method of direct injection is then the default solution chosen for the design of the system.

4. TOLERANCE ANALYSIS

Using the design previously presented and realized on Zemax, the tolerance analysis aims at testing the tolerance for each optics and assessing the impact of misalignments, surfaces qualities and other optical errors on the coupling efficiency with the chip. The objective is to decide which optics can be used for the alignment procedure and to meet the requirements stated in Sec. 2.3. To assess this impact, the coupling efficiency defined in Eq. 2 is calculated for each of the four inputs directly with Zemax.

4.1 Optical misalignment

4.1.1 Optimal coupling efficiency on Zemax

Using the tools on Zemax to compute the coupling efficiency for each of the four beams in the case of a perfect alignment, we obtain

$$\begin{cases} \rho_1 = 0.800 \text{ (blue beam in Fig. 3)} \\ \rho_2 = 0.798 \text{ (green beam in Fig. 3)} \\ \rho_3 = 0.800 \text{ (red beam in Fig. 3)} \\ \rho_4 = 0.798 \text{ (yellow beam in Fig. 3)} \end{cases}. \tag{11}$$

The different coupling efficiencies come from the difference in aberration between the beams closer to the optical axis (blue and red beams) and those closer to the edges of the lenses (green and yellow ones) in Fig. 3. If we consider a symmetric intensity between the four beams, then the relative intensity error induced by the difference in coupling efficiency alone is $\sigma_I \simeq 0.125\%$ which is smaller than the 1% requirements mentioned in Sec. 2.4.2 for a null depth of $N < 10^{-4}$. This divergence $< 1\%$ in the coupling efficiency is the benefit of the telecentric system that is implemented.

4.1.2 Impact of misalignment on coupling efficiency

Three optics are studied in the tolerance analysis to observe the impact of their misalignment on the coupling efficiency. For each of these optics, we study the worst beam in terms of coupling efficiency which corresponds to the green beam (or the yellow beam that is symmetric) in Fig. 3 and we estimate the precision required to have a coupling efficiency $> 75\%$ as mentioned in the requirements (see Sec. 2.3).

Slicer or IIP mirrors:
With regards to their position in the IIP, the mirrors misalignment is only acting on the pupil position with regards to the cold stop and not on the spot position in the image plane. A pupil misalignment therefore results in a loss of energy coupled with the chip combiner. Fig. 6 shows that a precision of $\sim 800\,\mu\text{rad}$ is required to have a coupling efficiency $> 75\%$. The IIP mirrors are planned to be manufactured as a monolithic system with fixed positions for the mirrors.
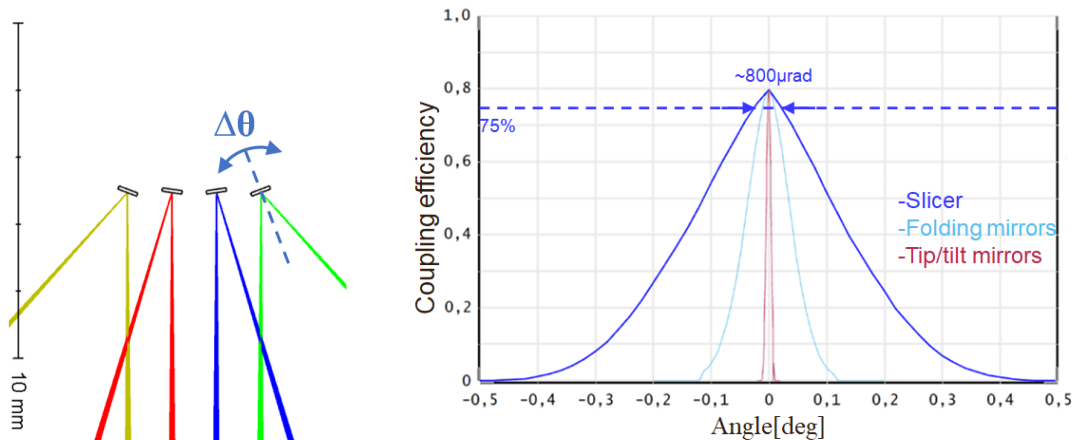

Figure 6. (left) Example of tilt angle for a slicer mirror. (right) Energy coupling with the chip input depending on the tilt angle of the slicer mirror as simulated on Zemax for the green beam.

<u>Folding mirrors:</u>
Folding mirrors are located in an intermediate plane between the IIP and the pupil plane of the system. They are then acting both on the pupil position with regards to the cold stop and the spot position in the image plane. The energy loss in the injection may therefore be caused by both misalignments. The precision required for a coupling efficiency > 75 % is about 450 µrad as plotted in Fig. 7.
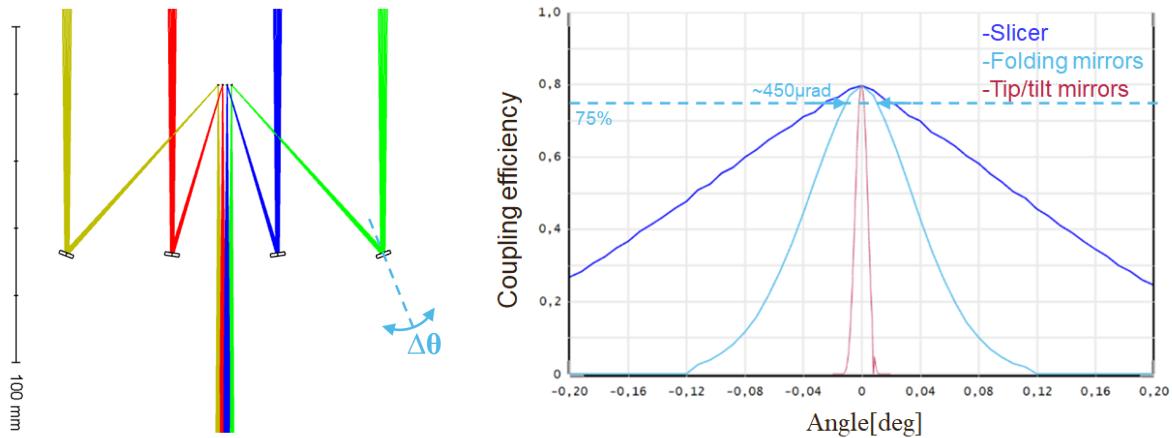

Figure 7. (left) Example of tilt angle for a folding mirror. (right) Energy coupling with the chip input depending on the tilt angle of the folding mirror as simulated on Zemax for the green beam.

<u>Tip/tilt mirrors:</u>
Tip/tilt mirrors are located in the pupil plane before the OAP of the system. They are acting on the spot position of each beam in the image plane without changing the pupil position with regards to the cold stop. The precision required for a coupling efficiency > 75 % is about 50 µrad as shown in Fig. 8.
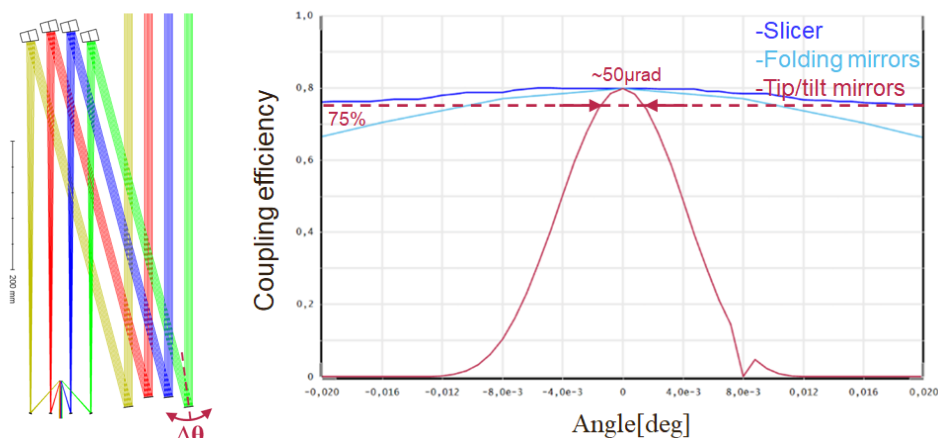

Figure 8. (left) Example of tilt angle for a Tip/tilt mirror. (right) Energy coupling with the chip input depending on the tilt angle of the Tip/tilt mirror as simulated on Zemax.

4.1.3 Alignment procedure

The alignment of the injection system requires both spot alignment in the image plane with the inputs of the chip and pupil alignment between the pupil plane and the cold stop. The optimal solution would be to use the IIP mirrors to align only the pupil planes while the tip/tilt mirrors would align the spots in the image plane. However, the IIP mirrors are planned to be fixed in the design with a monolithic design. Therefore, the pupil

alignment needs to be performed by the folding mirrors in association with the tip/tilt mirrors to maintain the coupling efficiency above 75 % for all individual inputs.

4.2 Surface quality

4.2.1 Impact of surface errors on coupling efficiency

Surface imperfections are generating wavefront errors which result in aberrations when focusing the beam in the image plane. The aberrations are hampering the coupling efficiency with the chip input. This energy loss from wavefront aberrations can be approximated by the Strehl ratio which represents the ratio of peak diffraction intensities between an aberrated and a perfect wavefront. For small aberrations (normalized wavefront error $\omega \leq 1/10\,\text{RMS}$), this Strehl ratio S can be calculated using Maréchal's approximation:

$$S \sim e^{-(2\pi\omega)^2} \tag{12}$$

with the normalized wavefront error RMS ω corresponding to

$$\omega = \frac{\lambda_{ref}}{N} \cdot \frac{1}{\lambda} \tag{13}$$

with λ_{ref} the reference wavelength (usually $\lambda_{ref} = 633\,\text{nm}$), N the integer for surface quality and λ the central wavelength of the beam ($\lambda = 3.8\,\mu\text{m}$ in this case). A mirror with a reflected wavefront error (RWE) RMS of $\frac{\lambda_{ref}}{4}$ then has $\omega \simeq 0.0416$ at $\lambda = 3.8\,\mu\text{m}$ which then leads to a Strehl ratio $S \simeq 93.4\,\%$. For a multiple optics combination, the total Strehl ratio of such a system with a number of optics N_{optics} is

$$S \sim e^{-(2\pi\omega_t)^2} \tag{14}$$

$$\text{with:} \quad \omega_t = \sqrt{\sum_i^{N_{\text{optics}}} \omega_i^2}. \tag{15}$$

In the case of OAP mirrors, the surface quality is already given in RWE RMS. While for plane mirrors, the information is given in terms of surface flatness Peak-to-Valley (P-V): ω_{flat}. To convert the value of ω_{flat} into a wavefront error RMS, the following relations are used:

$$\begin{cases} \omega_{\text{best}} = 2\omega_{\text{flat}} \cdot \frac{1}{3.5} \\ \omega_{\text{worst}} = 2\omega_{\text{flat}} \end{cases}. \tag{16}$$

The factor 2 enables to convert the surface flatness into wavefront errors. The conversion from P-V to RMS is trickier because no exact solution exists: in the best case scenario, the mirror has a single broad smooth defect allowing a factor 1/3.5 to be applied for conversion. In the worst case scenario, the P-V measurement is equivalent to the RMS and no additional factor is then applied for the conversion. Because a RMS value is a statistic measurement for the entire optical surface, it contains more information than a P-V measurement, explaining this uncertainty in the conversion.

4.2.2 Impact of surface errors on null depth

Even though the use of waveguides relaxes the constraints on surface quality by filtering the wavefront, the RWE may still translate into a relative intensity error. The RWE are indeed generating an uncertainty in the coupling efficiency for each beam that is translated to a photometric relative unbalance, which then hampers the null depth capacity of the instrument. This null depth is calculated from the normalized wavefront error RMS ω obtained in Eq. 14 following the formula from[24]

$$N = \frac{(2\pi\omega)^4}{16}. \tag{17}$$

Similarly to the requirements listed in Sec. 2, to allow a total raw null depth $< 10^{-3}$ for the instrument, the contribution from the surface errors should give a null depth $\leq 10^{-4}$ as a safe margin.

4.2.3 Requirements on surface quality

The current injection system design lists four reflective optics susceptible to generate wavefront errors on each beam: three plane mirrors (tip/tilt, folding and slicer/IIP mirrors) and an OAP mirror. The surface quality for the two lenses in the telecentric system are not taken into account in this calculation. The RWE RMS of OAP are generally estimated at $\frac{\lambda}{4}$ @633 nm. Using Eq. 14 and Eq. 17, the mean Strehl ratio and mean null depth can be calculated depending on the number of plane mirrors and their surface flatness in Fig. 9.
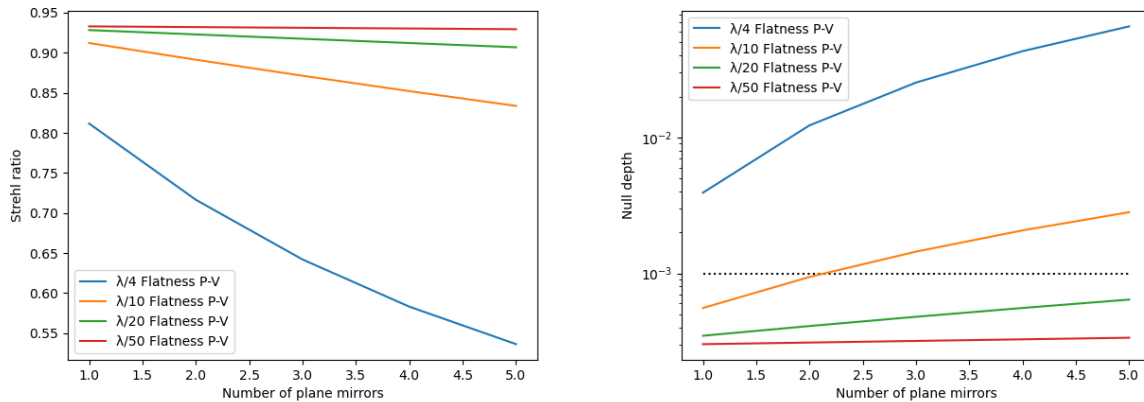

Figure 9. (left) Strehl ratio and (right) null depth at $\lambda = 3.8\,\mu$m with respect to the number of plane mirrors and their associated surface flatness P-V. An OAP with RWE $\frac{\lambda}{4}$ @633 nm RMS is considered in addition.

The maximum surface flatness for three plane mirrors is $\frac{\lambda}{20}$ @633 nm to have a null depth below 10^{-3}, however this is not sufficient to ensure a safe margin with a null depth of $> 10^{-4}$ as mentioned in Sec. 4.2.2. Moreover, a minimum Strehl ratio of 95 % is also required to have a coupling efficiency > 75 % which is prevented mainly by the surface quality of the OAP. Optics with higher surface quality then have to be considered to satisfy the requirements for both the coupling efficiency and the intensity error. If we consider the same simulation with a RWE RMS of $\frac{\lambda}{10}$ @633 nm for the OAP, we obtain the results in Fig. 10.
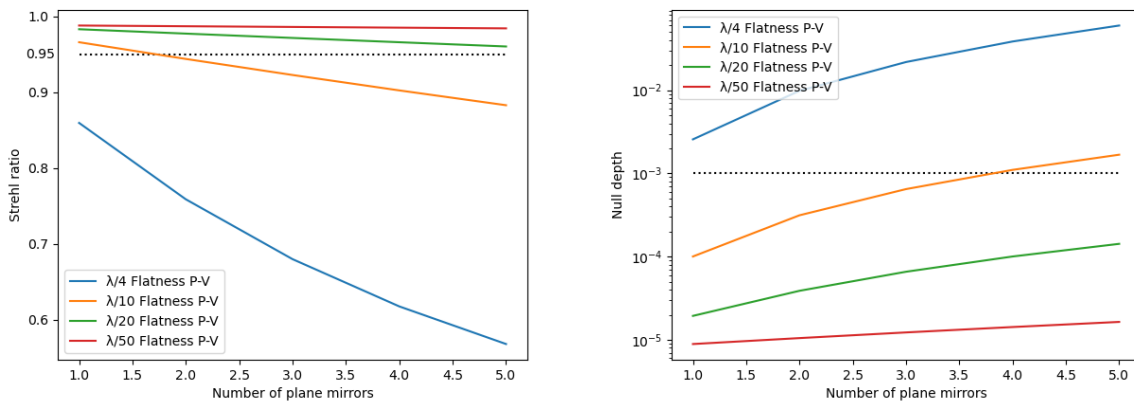
Figure 10. (left) Strehl ratio and (right) null depth at $\lambda = 3.8\,\mu$m with respect to the number of plane mirrors and their associated surface flatness P-V. An OAP with RWE $\frac{\lambda}{10}$ @633 nm RMS is also considered.

The minimum surface quality required to achieve both a Strehl ratio > 95 % and a null depth $< 10^{-4}$ corresponds to plane mirrors with a surface flatness of $\frac{\lambda}{20}$ @633 nm and a RWE RMS of $\frac{\lambda}{10}$ @633 nm for the OAP.

For three plane mirrors at $\lambda = 3.8\,\mu\text{m}$, this gives the following values:

$$\begin{cases} S \simeq 97\,\% \\ N \simeq 6.6 \times 10^{-5} \end{cases} \tag{18}$$

which are in agreement with the requirements.

4.3 Other errors impact on coupling efficiency and intensity errors

In order to respect the requirement of $1\,\%$ relative intensity error demonstrated in Sec. 2.4.2 compared to the coupling efficiency of $80\,\%$ from Eq. 11, a minimum coupling efficiency of $78.3\,\%$ for each individual input is required on Zemax, and will be used as reference for the following analysis. At the end of the section, the Strehl ratio from Eq. 18 is applied to ensure that each individual coupling efficiency is at least $75\,\%$.

4.3.1 Impact of OAP focal length error

The precision on the OAP focal length must not degrade the coupling efficiency and cause an intensity difference between the inputs of the chip. Taking a focal length error of $\pm0.1\,\%$ gives the results in Table. 1.

Inputs	-0.1 %	0	+0.1 %
ρ_1	0.794	0.800	0.799
ρ_1	0.798	0.798	0.797
ρ_1	0.797	0.800	0.796
ρ_1	0.799	0.798	0.798

Table 1. Coupling efficiency between the four beams and their respective inputs in the chip combiner for the ideal OAP effective focal length and the maximum associated errors $\pm0.1\,\%$.

4.3.2 Impact of the cold stop position error

The cold stop position at the pupil plane ensures that the system remains telecentric as stated in Sec. 3. The results in Table. 2 are obtained for a cold stop position error of $\pm2\,\text{mm}$.

Inputs	-2 mm	0	+2 mm
ρ_1	0.797	0.800	0.800
ρ_1	0.798	0.798	0.798
ρ_1	0.800	0.800	0.794
ρ_1	0.799	0.798	0.796

Table 2. Coupling efficiency between the four beams and their respective inputs in the chip combiner for the ideal cold stop position and the maximum associated errors $\pm2\,\text{mm}$.

4.3.3 Impact of the telecentric lens focal length error

The focal length of the telecentric lens is critical for the injection of the four beams into the chip. The results in Table. 3 are obtained for an error of $\pm0.1\,\%$.

Inputs	-0.1 %	0	+0.1 %
ρ_1	0.803	0.800	0.792
ρ_1	0.797	0.798	0.796
ρ_1	0.803	0.800	0.792
ρ_1	0.797	0.798	0.796

Table 3. Coupling efficiency between the four beams and their respective inputs in the chip combiner for the ideal focal length of the telecentric lens and the maximum associated errors $\pm0.1\,\%$.

4.3.4 Impact of all the optical errors

From the results in Table. 1-3, the most critical case for the system coupling efficiency corresponds to an OAP focal length error of $+0.1\%$, a telecentric lens focal length error of $+0.1\%$ and a pupil position error of $+2\,\mathrm{mm}$. This gives the following total individual coupling efficiencies for the four inputs:

$$\begin{cases} \rho_1 = 0.791 \\ \rho_2 = 0.794 \\ \rho_3 = 0.784 \\ \rho_4 = 0.794 \end{cases}. \tag{19}$$

Considering the Strehl ration from Eq. 18 of 97% and the results from Eq. 19, the total minimum coupling efficiencies of the system for the four inputs is

$$\begin{cases} \rho_1 = 0.767 \\ \rho_2 = 0.770 \\ \rho_3 = 0.760 \\ \rho_4 = 0.770 \end{cases}. \tag{20}$$

These results respect the requirements in terms of relative intensity error. The surface quality and optical errors mentioned in this section have to be discussed with manufacturers to assess their feasibility.

5. CONCLUSION

In this work, a first version of the Hi-5 fiber-free injection system coupling the four VLTI beams into a L-band photonic chip is presented. The main guidelines to be respected are a coupling efficiency $\rho > 75\%$ and a raw null depth $N \leq 10^{-3}$, which sets the maximum relative intensity errors at approximately 1% between the four beams. We demonstrate that the design implemented on Zemax, composed of two telecentric system lenses and a pupils combiner (slicer), satisfies those requirements. A tolerance analysis is then performed to assess the impact of mirrors misalignment both on the pupil and image planes. We identified that to achieve a coupling efficiency of $\rho > 75\%$, the adjustment of two degrees of freedom is needed, and we selected the folding mirrors and the tip/tilt mirrors as possible motorized actuated controls. Their angle precision amounts to about $450\,\mathrm{\mu rad}$ for the folding mirrors and $50\,\mathrm{\mu rad}$ for the tip/tilt mirrors. The impact of the reflected wavefront errors due to the OAP and flat mirrors surface quality is also investigated, as it contributes to degrade both the coupling efficiency and the null depth. The results show that a RWE of at most $\frac{\lambda}{10}$ @633 nm RMS for the OAP and a surface flatness of at most $\frac{\lambda}{20}$ @633 nm P-V for the plane mirrors are necessary to fulfill the requirements. Finally, we suggest that to respect a relative intensity error of at least 1%, the OAP focal length error, the cold stop position tolerance and the injection lens focal length precision should be respectively limited to $\pm 0.1\%$, $\pm 2\,\mathrm{mm}$, and $\pm 0.1\%$.

6. FUTURE WORK

As the Hi-5 warm optics design develops towards a compute system, the next step is its integration into the Asgard suite. The beams will enter into Hi-5 after L/K band dichroic mirrors shared with Heimdallr, a high-sensitivity K-band fringe tracker[8]. The combination will be done respecting the optical path length, the space constraints, the throughput, and the pupil matching between the two systems. Secondly, a pupil and image control by an alignment camera will be added before the chip, back-illuminated with a powerful source. This configuration is being tested now in the laboratory. In parallel, we will discuss with manufacturers the feasibility of the optics with the required properties and surface quality. This will lead to update the tolerance budget (for example, the lenses quality has not yet been considered). As a subsequent control, an evaluation of the polarization mismatch will be performed to quantify its impact on the null depth. Finally, the system will be implemented and tested in the laboratory.

ACKNOWLEDGMENTS

REFERENCES

[1] Fulton, B. J., Rosenthal, L. J., Hirsch, L. A., Isaacson, H., Howard, A. W., Dedrick, C. M., Sherstyuk, I. A., Blunt, S. C., Petigura, E. A., Knutson, H. A., Behmard, A., Chontos, A., Crepp, J. R., Crossfield, I. J. M., Dalba, P. A., Fischer, D. A., Henry, G. W., Kane, S. R., Kosiarek, M., Marcy, G. W., Rubenzahl, R. A., Weiss, L. M., and Wright, J. T., "California Legacy Survey. II. Occurrence of Giant Planets beyond the Ice Line," *The Astrophysical Journal Supplement Series* **255**, 14 (July 2021).

[2] GRAVITY Collaboration, Lacour, S., Nowak, M., Wang, J., Pfuhl, O., Eisenhauer, F., Abuter, R., Amorim, A., Anugu, N., Benisty, M., Berger, J. P., Beust, H., Blind, N., Bonnefoy, M., Bonnet, H., Bourget, P., Brandner, W., Buron, A., Collin, C., Charnay, B., Chapron, F., Clénet, Y., Coudé du Foresto, V., de Zeeuw, P. T., Deen, C., Dembet, R., Dexter, J., Duvert, G., Eckart, A., Förster Schreiber, N. M., Fédou, P., Garcia, P., Garcia Lopez, R., Gao, F., Gendron, E., Genzel, R., Gillessen, S., Gordo, P., Greenbaum, A., Habibi, M., Haubois, X., Haußmann, F., Henning, T., Hippler, S., Horrobin, M., Hubert, Z., Jimenez Rosales, A., Jocou, L., Kendrew, S., Kervella, P., Kolb, J., Lagrange, A.-M., Lapeyrère, V., Le Bouquin, J.-B., Léna, P., Lippa, M., Lenzen, R., Maire, A.-L., Mollière, P., Ott, T., Paumard, T., Perraut, K., Perrin, G., Pueyo, L., Rabien, S., Ramírez, A., Rau, C., Rodríguez-Coira, G., Rousset, G., Sanchez-Bermudez, J., Scheithauer, S., Schuhler, N., Straub, O., Straubmeier, C., Sturm, E., Tacconi, L. J., Vincent, F., van Dishoeck, E. F., von Fellenberg, S., Wank, I., Waisberg, I., Widmann, F., Wieprecht, E., Wiest, M., Wiezorrek, E., Woillez, J., Yazici, S., Ziegler, D., and Zins, G., "First direct detection of an exoplanet by optical interferometry: Astrometry and K-band spectroscopy of HR 8799 e," *Astronomy & Astrophysics* **623**, L11 (Mar. 2019).

[3] Bracewell, R. N., "Detecting nonsolar planets by spinning infrared interferometer," *Nature* **274**, 780–781 (Aug. 1978).

[4] Serabyn, E., Mennesson, B., Martin, S., Liewer, K., and Kühn, J., "Nulling at short wavelengths: theoretical performance constraints and a demonstration of faint companion detection inside the diffraction limit with a rotating-baseline interferometer," *Monthly Notices of the Royal Astronomical Society* **489**, 1291–1303 (Oct. 2019).

[5] Colavita, M. M., Serabyn, E., Millan-Gabet, R., Koresko, C. D., Akeson, R. L., Booth, A. J., Mennesson, B. P., Ragland, S. D., Appleby, E. C., Berkey, B. C., Cooper, A., Crawford, S. L., Creech-Eakman, M. J., Dahl, W., Felizardo, C., Garcia-Gathright, J. I., Gathright, J. T., Herstein, J. S., Hovland, E. E., Hrynevych, M. A., Ligon, E. R., Medeiros, D. W., Moore, J. D., Morrison, D., Paine, C. G., Palmer, D. L., Panteleeva, T., Smith, B., Swain, M. R., Smythe, R. F., Summers, K. R., Tsubota, K., Tyau, C., Vasisht, G., Wetherell, E., Wizinowich, P. L., and Woillez, J. M., "Keck Interferometer Nuller Data Reduction and On-Sky Performance," *Publications of the Astronomical Society of the Pacific* **121**, 1120–1138 (Oct. 2009).

[6] Hinz, P., Solheid, E., Durney, O., and Hoffmann, W., "Nic: Lbti's nulling and imaging camera," *Proceedings of SPIE - The International Society for Optical Engineering* **7013** (07 2008).

[7] Defrère, D., Absil, O., Berger, J.-P., Bigioli, A., Courtney-Barrer, B., Dandumont, C., Emsenhuber, A., Ertel, S., Gagne, J., Garreau, G., Glauser, A., Gross, S., Ireland, M., Kenchington, H.-D., Kraus, S., Labadie, L., Laborde, V., Laugier, R., Leisenring, J., Loicq, J., Martin, G., Martinache, F., Martinod, M.-A., Matter, A., Mazzoli, A., Mennesson, B., Salman, M., Raskin, G., Vandenbussche, B., Verlinden, S., and Woillez, J., "L-band nulling interferometry at the VLTI with ASGARD/Hi-5: status and plans," in [*Optical and Infrared Interferometry and Imaging VIII*], *Society of Photo-Optical Instrumentation Engineers (SPIE) Conference Series* **12183**, 12183–16 (July 2022).

[8] Martinod, M.-A., Bigioli, A., Bryant, J., Chhabra, S., Courtney-Barrer, B., Crous, F., Cvetojevic, N., Dandumont, C., Defrère, D. Garreau, G., Ireland, M., Kraus, T., Lagadec, T., Laugier, R., Martinache, F., Mortimer, D., Norris, B., Robertson, G., Taras, A., and Tuthill, P. G., "High-angular and high-contrast VLTI observations from J to M band with the Asgard instrumental suite," in [*Optical and Infrared Interferometry and Imaging VIII*], *Society of Photo-Optical Instrumentation Engineers (SPIE) Conference Series* **12183**, 12183–36 (July 2022).

[9] Defrère, D., Ireland, M., Absil, O., Berger, J.-P., Danchi, W. C., Ertel, S., Gallenne, A., Hénault, F., Hinz, P., Huby, E., Kraus, S., Labadie, L., Bouquin, J.-B. L., Martin, G., Matter, A., Mennesson, B., Mérand, A., Minardi, S., Monnier, J. D., Norris, B., de Xivry, G. O., Pedretti, E., Pott, J.-U., Reggiani, M., Serabyn, E., Surdej, J., Tristram, K. R. W., and Woillez, J., "Hi-5: a potential high-contrast thermal near-infrared imager for the VLTI," in [*Optical and Infrared Interferometry and Imaging VI*], Creech-Eakman, M. J., Tuthill, P. G., and Mérand, A., eds., **10701**, 223 – 237, International Society for Optics and Photonics, SPIE (2018).

[10] Berger, J.-P., Zins, G., Lazareff, B., Lebouquin, J., Jocou, L., Kern, P., Millan-Gabet, R., Traub, W., Haguenauer, P., Absil, O., Augereau, J.-C., Benisty, M., Blind, N., Bonfils, X., Delboulbé, A., Feautrier, P., Germain, M., Gillier, D., Gitton, P., and Tatulli, E., "Pionier: a visitor instrument for the vlti," *Proceedings of SPIE - The International Society for Optical Engineering* **7734** (08 2010).

[11] Martinod, M.-A., Norris, B., Tuthill, P., Lagadec, T., Jovanovic, N., Cvetojevic, N., Gross, S., Arriola, A., Gretzinger, T., Withford, M. J., Guyon, O., Lozi, J., Vievard, S., Deo, V., Lawrence, J. S., and Leon-Saval, S., "Scalable photonic-based nulling interferometry with the dispersed multi-baseline GLINT instrument," *Nature Communications* **12**, 2465 (Dec. 2021).

[12] Sanny, A., Labadie, L., Gross, S., Defrère, D., Bigioli, A., Laugier, R., Gretzinger, T., and Withford, M., "Development of the 4-telescope photonic nuller of Hi-5 for the characterization of exoplanets in the mid-IR," in [*Optical and Infrared Interferometry and Imaging VIII*], *Society of Photo-Optical Instrumentation Engineers (SPIE) Conference Series* **12183**, 12183–43 (July 2022).

[13] Labadie, L., Minardi, S., Tepper, J., Diener, R., Muthusubramanian, B., Pott, J.-U., Nolte, S., Gross, S., Arriola, A., and Withford, M. J., "Photonics-based mid-infrared interferometry: 4-year results of the ALSI project and future prospects," (Mar. 2020). arXiv:2003.02582 [astro-ph].

[14] Gretzinger, T., Gross, S., Arriola, A., and Withford, M. J., "Towards a photonic mid-infrared nulling interferometer in chalcogenide glass," *Optics Express* **27**, 8626 (Mar. 2019).

[15] Ireland, M. J., Defrère, D., Martinache, F., Monnier, J., Woillez, J., Tuthill, P. G., and Norris, B., "Image-plane fringe tracker for adaptive-optics assisted long baseline interferometry," in [*Optical and Infrared Interferometry and Imaging VI*], Mérand, A., Creech-Eakman, M. J., and Tuthill, P. G., eds., 21, SPIE, Austin, United States (July 2018).

[16] V. Coudé du Foresto, Ridgway, S., and Mariotti, J.-M., "Deriving object visibilities from interferograms obtained with a fiber stellar interferometer," *Astronomy and Astrophysics Supplement Series* **121**, 379–392 (Feb. 1997).

[17] Ruilier, C., "Filtrage modal et recombinaison de grands télescopes. contributions à l'instrument fluor," (01 1999).

[18] Laugier, R., Defrère, D., Matter, A., Courtney-Barrer, B., Gross, S., Dannert, F., Woillez, J., Bigioli, A., Absil, O., and Dandumont, C., "The expected performance of nulling at the VLTI down to 5 mas," in [*Optical and Infrared Interferometry and Imaging VIII*], *Society of Photo-Optical Instrumentation Engineers (SPIE) Conference Series* **12183**, 12183–76 (July 2022).

[19] Serabyn, E., "Nulling interferometry: symmetry requirements and experimental results," in [*Interferometry in Optical Astronomy*], Lena, P. J. and Quirrenbach, A., eds., **4006**, 328 – 339, International Society for Optics and Photonics, SPIE (2000).

[20] Lacour, S., Dembet, R., Abuter, R., Fédou, P., Perrin, G., Choquet, E., Pfuhl, O., Eisenhauer, F., Woillez, J., Cassaing, F., Wieprecht, E., Ott, T., Wiezorrek, E., Tristram, K., Wolff, B., Ramirez Molina, A., Haubois, X., Perraut, K., Straubmeier, C., and Amorim, A., "The gravity fringe tracker," *Astronomy and Astrophysics* **624** (04 2019).

[21] Absil, O., den Hartog, R., Gondoin, P., Fabry, P., Wilhelm, R., Gitton, P., and Puech, F., "Performance study of ground-based infrared bracewell interferometers - application to the detection of exozodiacal dust disks with genie," *A&A* **448**(2), 787–800 (2006).

[22] Coude du Foresto, V., Perrin, G. S., Ruilier, C., Mennesson, B. P., Traub, W. A., and Lacasse, M. G., "FLUOR fibered instrument at the IOTA interferometer," 856 (July 1998).

[23] Jocou, L., Perraut, K., Moulin, T., Magnard, Y., Labeye, P., Lapras, V., Nolot, A., Perrin, G., Eisenhauer, F., Holmes, C., Amorim, A., Brandner, W., and Straubmeier, C., "The beam combiners of Gravity VLTI instrument: concept, development, and performance in laboratory," 91461J (July 2014).

[24] Mennesson, B., Ollivier, M., and Ruilier, C., "Use of single-mode waveguides to correct the optical defects of a nulling interferometer," *Journal of the Optical Society of America A* **19**, 596 (Mar. 2002).